

New methods to compute the generalized chi-square distribution

Abhranil Das

abhranil.das@utexas.edu

Center for Perceptual Systems, and Center for Theoretical and Computational Neuroscience
The University of Texas at Austin

July 31, 2024

Abstract

We present several new mathematical methods (ray-trace, inverse Fourier transform and ellipse) and open-source software to compute the cdf, pdf and inverse cdf of the generalized chi-square distribution. Some methods are geared for speed, while others are designed to be accurate far into the tails, using which we can also measure large values of the discriminability index d' between multinormals. We characterize the performance and limitations of these and previous methods, and recommend the best methods to use for each part of each type of distribution. We also demonstrate the speed and accuracy of our new methods against previous methods across a wide sample of distributions.

code [on github](#)). Imhof²² used Gil-Pelaez's method²³ of inverting the characteristic function to compute the cdf and pdf for mixed w_i as well, but not with the normal term. Davies²⁴ extended the characteristic function to let Imhof's inversion work with the normal s term too, and we further incorporated the offset m and implemented it as `gx2cdf(..., 'method', 'imhof')` and `gx2pdf(..., 'method', 'imhof')` in our toolbox. This method requires computing an integral, and we provide the option to compute it fast with double precision numerics, or slowly but more accurately using variable precision arithmetic (vpa).

These exact methods all work well in the center of the distribution, but far into the tails they begin to reach their limits of accuracy or speed at different points. For this reason several approximations have been derived for the cdf, such as Imhof's extension²² of Pearson's approximation²⁵ (only usable when $s = 0$), and Liu et al's²⁶ and Zhang et al's²⁷ approximations (only usable when $\mathbf{q}_1 = 0$, i.e. $s = 0$, and \mathbf{Q}_2 is non-negative definite, i.e. when all w_i are the same sign). So these approximate methods are often only applicable to limited cases, and even then have their inaccuracies. See Zhang et al,²⁷ Duchesne et al²⁸ and Bodenham et al²⁹ for a review of these approximate methods and their limitations.

In this paper we first develop three new methods to compute the generalized chi-square cdf and pdf. These methods will have different tradeoffs, e.g. the inverse Fourier transform method is geared for speed, the ray-trace method is slower but accurate far into the tails, and the ellipse method is a fast approximation that becomes exact in the finite tail. Then we compare their performances on computing the cdf and pdf against existing exact methods. We show that together, they let us reach extremely small values in all tails of all types of generalized chi-square distributions, and we provide a table of the best method to use in each case. Next, we show further accuracy tests of the new methods by: (i.) replicating previously published cdf values, (ii.) by measuring the accuracy of our cdf and pdf methods against previous exact methods, and also the accuracy of our inverse cdf method, over a wide sample of distributions, and (iii) by computing high values of the discriminability index d' between two multinormals that can be checked by a simpler calculation.

1 Introduction

The generalized chi-square variable $\tilde{\chi}$ is a quadratic form of a d -dimensional multinormal variable $\mathbf{x} \sim N(\boldsymbol{\mu}, \boldsymbol{\Sigma})$, and can also be seen as a weighted sum of non-central chi-square variables χ'^2 and a standard normal variable z :

$$\begin{aligned}\tilde{\chi}_{\mathbf{w}, \mathbf{k}, \boldsymbol{\lambda}, s, m} &= q(\mathbf{x}) = \mathbf{x}' \mathbf{Q}_2 \mathbf{x} + \mathbf{q}'_1 \mathbf{x} + q_0 \\ &= \sum_i w_i \chi'^2_{k_i, \lambda_i} + sz + m.\end{aligned}$$

(Regular symbols are scalars, bold lowercase symbols are column vectors, and bold uppercase symbols are matrices.)

This distribution arises across many fields, such as statistics and machine learning,^{1–6} neuroscience,⁷ cosmology,^{8,9} signal transmission,^{10–12} satellite navigation,^{13,14} quality control,¹⁵ cybersecurity¹⁶ and robotics.^{17–20}

When $s = 0$ and w_i are all positive or all negative, the quadratic is an ellipse. Then the distribution starts from the finite point m at one end, which can be called a finite tail, and the other end tails off at $+$ or $-\infty$ respectively, which we call an infinite tail. When w_i have mixed signs, and/or there is a normal s term, both tails are infinite.

There are several existing methods to compute the cdf and pdf of this distribution, which may behave differently in finite vs. infinite tails. When all w_i are the same sign and $s = 0$, i.e. the quadratic is an ellipse, Ruben's method²¹ can be used to compute the cdf, implemented as `gx2cdf(..., 'method', 'ruben')` in our Matlab toolbox '[Generalized chi-square distribution](#)' (source

2 Mapping to a quadratic form

We had previously shown how to map from the parameters of a multinormal and the coefficients of its quadratic form to the parameters of the resulting generalized chi-square distribution⁷ (function `norm_quad_to_gx2_params` in our toolbox). As a first step to some of our methods, it will help to find the inverse map, i.e. from the parameters of a generalized chi-square distribution to the parameters of a multinormal and its quadratic form. This inverse map is one-to-many: there are infinite pairs of multinormals and corresponding quadratics that have the same distribution. So, in order to arrive at a single solution, we shall consider a canonical form where the multinormal is the standard normal, and find a quadratic form of it that will produce the given generalized chi-square distribution.

Let us start from an example. Suppose the generalized chi-square parameters are weights $\mathbf{w} = [w_1 \ w_2 \ w_3]$, degrees of freedom $\mathbf{k} = [1 \ 1 \ 2]$, non-centralities $\boldsymbol{\lambda} = [\lambda_1 \ \lambda_2 \ \lambda_3]$, and linear coefficients s and m . We build this as a sum of squares of independent scaled and shifted standard normal variables z_i , plus a linear term. For any term with multiple degrees of freedom, we split it into as many standard normals, choosing to put the entire non-centrality in the first term. So in this case we have the quadratic as:

$$q(\mathbf{z}) = w_1(z_1 - \sqrt{\lambda_1})^2 + w_2(z_2 - \sqrt{\lambda_2})^2 + w_3\{(z_3 - \sqrt{\lambda_3})^2 + z_4^2\} + sz_5 + m. \quad (1)$$

Now let us express the quadratic in vector and matrix notation: $q(\mathbf{z}) = \mathbf{z}'\mathbf{Q}_2\mathbf{z} + \mathbf{q}'_1\mathbf{z} + q_0$, where \mathbf{z} is a standard normal vector, \mathbf{Q}_2 is a square matrix, and \mathbf{q}_1 is a vector. First consider $s = 0$. Then the standard normal has $\sum k_i$ dimensions. Collecting the second order terms, we can see that the matrix \mathbf{Q}_2 is diagonal, here $[w_1 \ w_2 \ w_3 \ w_3]$, i.e. in general it is constructed by appending each $w_i \ k_i$ times. Then collecting the linear z_i terms, we see that $\mathbf{q}'_1 = [-2w_1\sqrt{\lambda_1} \ -2w_2\sqrt{\lambda_2} \ -2w_3\sqrt{\lambda_3} \ 0]$, i.e. in general we append each $-2w_i\sqrt{\lambda_i}$, followed by a 0 $k_i - 1$ times. And $q_0 = \sum w_i\lambda_i + m$. Now when $s \neq 0$, we increase the dimension to $\sum k_i + 1$, append the diagonal \mathbf{Q}_2 with a 0, and append \mathbf{q}_1 with s . This mapping is available as function `gx2_to_norm_quad_params` in our toolbox.

Given any quadratic form of any multinormal, we can simplify it by first finding its generalized chi-square parameters, then mapping back to this canonical quadratic of the standard multinormal.

Even though in this inverse map we fix the multinormal to be the unit sphere, this is still not its only quadratic function that has the given distribution. What is the entire family of inverse maps? First, in a term with multiple degrees of freedom, we could split the total non-centrality in any way, which corresponds to rotating the quadratic around the origin in that sub-space. Second, we can apply any linear transform to the entire space where the multinormal and the quadratic lives. So we can spherically rotate the quadratic around the origin without changing the distribution, and finally we can scale and shift the space so that the multinormal is no longer standard.

By mapping from generalized chi-square parameters to quadratic coefficients, then sampling standard normal vectors and computing their quadratic form, we can sample from the gener-

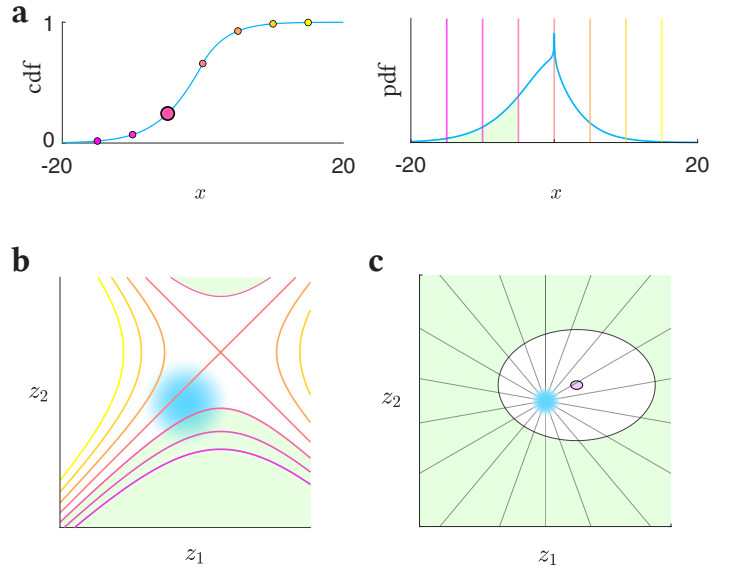


Figure 1: Mapping from the generalized chi-square parameters to the quadratic form of a multinormal, and integrating using ray-trace. **a.** A generalized chi-square cdf at one of several points (left, larger dot) is the pdf integrated upto that point (right, green area). **b.** This integrated probability corresponds to the standard multinormal (blue blob) probability over a domain (green area) that belongs to a family of quadratics (colours in this family correspond across plots a-b). **c.** The lower (finite) and upper (infinite) tail cdf of a generalized chi-square that corresponds to a non-central ellipse, are the standard multinormal (blue blob) probability inside the tiny ellipse (purple area) and outside the large ellipse (green area) respectively. All rays emanating from the normal hit the large ellipse, but most miss the small one.

alized chi-square distribution (function `gx2rnd` in our toolbox). This is an alternative to sampling from the constituent noncentral chi-squares and a normal and adding them.

Fig. 1a shows the cdf of a generalized chi-square distribution with $\mathbf{w} = [1 \ -1]$, $\mathbf{k} = [1 \ 1]$, $\boldsymbol{\lambda} = [2 \ 4]$, $s = m = 0$. To compute the cdf, we can first map these parameters to the corresponding quadratic form of a bivariate standard normal, $\tilde{\chi} = q(\mathbf{z}) = z_1^2 - z_2^2 - 2\sqrt{2}z_1 + 4z_2 - 2$, a hyperbolic function. The cdf at a point $F(c) = p(\tilde{\chi} < c) = p(q(\mathbf{z}) < c)$ is then the multinormal probability within the contour of $q(\mathbf{z})$ at level c , i.e. the green area defined by the hyperbola $q(\mathbf{z}) < c$ or $q(\mathbf{z}) - c < 0$, fig. 1b. The cdf at other points are the probabilities within the other hyperbolas in this family as we vary c . These probabilities can be integrated in the \mathbf{z} -space with the ray-tracing method, as described in the following section.

3 Ray-tracing

3.1 Computing the cdf

Once we map from the generalized chi-square parameters to the quadratic form of a standard normal vector, we can now use the ray-tracing method⁷ to compute the cdf, available in our toolbox as `gx2cdf(..., 'method', 'ray')`. This is a method to compute the multinormal probability over arbitrary domains, including quadratic domains, for which it is especially fast and accurate.

In this method, we first linearly transform the space so that the distribution is the standard (unit spherical) multinormal. Then we send ‘rays’ out from its center at every angle, and find the distances where each ray hits the integration domain, analogous to the ray-tracing method of rendering computer graphics. Using these intersection distances, we analytically integrate the density along each ray, which we then numerically integrate across all the rays. In Matlab we can use grid integration across rays for up to 4 dimensions, and Monte-Carlo integration above that (or even in general), which automatically runs in parallel on a GPU when present.

The ray method uses careful strategies to preserve precision and compute probabilities down to about 10^{-308} , the smallest value expressible in double precision (called `realmin`). This is already a small enough probability for most imaginable applications. But for those beyond imagination, we provide a `vpa` option that can be turned on to implement the calculations symbolically, and evaluate the result with variable precision. (This works only with Monte-Carlo integration across rays, not with Matlab’s native grid integration.) When the `vpa` setting is off, if the method detects rays that cross the integration domain, yet the double-precision probability on them are 0, it notifies the user to turn on `vpa` if they want to include those small probabilities. With `vpa`, ray-tracing can be extended to compute probabilities smaller than `realmin`, all the way down to the absurdly small scale of about $10^{-3 \times 10^8}$, where Matlab’s symbolic calculation engine fails, so let us call this `symmin`. We believe that nobody should ever need this level of precision, in the same way that Bill Gates allegedly said that nobody should need more than 640KB of computer memory.

However, there is one situation in which the ray method cannot reach such small tail probabilities. When all w_i are the same sign, $\sum \lambda_i > 0$ (i.e. the constituent chi-squares are not all central) and $s = 0$, the corresponding quadratic form is an ellipse that is not at the origin. For example, consider $\tilde{\chi} = 2\chi_{k=1, \lambda=4}^{\prime 2} + 4\chi_{k=1, \lambda=1}^{\prime 2}$. This corresponds to the elliptical quadratic form: $\tilde{\chi} = q(z) = 2(z_1 - 2)^2 + 4(z_2 - 1)^2$ of the bivariate standard normal (fig. 1c). The lower (finite) tail probability $F(c) = p(q(z) < c)$, where c is small, is the standard normal probability inside a tiny off-set elliptical region (purple area), whereas the upper (infinite) tail probability $p(\tilde{\chi} > c)$, where c is large, is the probability outside a large elliptical region (green area). When we send rays from the normal center to compute the upper tail probability, they all hit the large domain and return small values that accurately sum to the small upper tail probability. But in the lower tail, most rays miss the tiny elliptical domain. If the domain is very tiny, no ray may hit it, and the cdf will be incorrectly computed as 0. In ≤ 4 dimensions, Matlab’s adaptive grid integral can, to some extent, automatically find the tiny domain and populate the grid densely there and avoid this problem, but beyond 4 dimensions, randomly sampled Monte-Carlo rays will all miss a small enough domain. Therefore, the ray method is not the best for this situation, and we will develop the ellipse approximation that works well in this case. When the chi-square components are all central, the ray method does not have this problem.

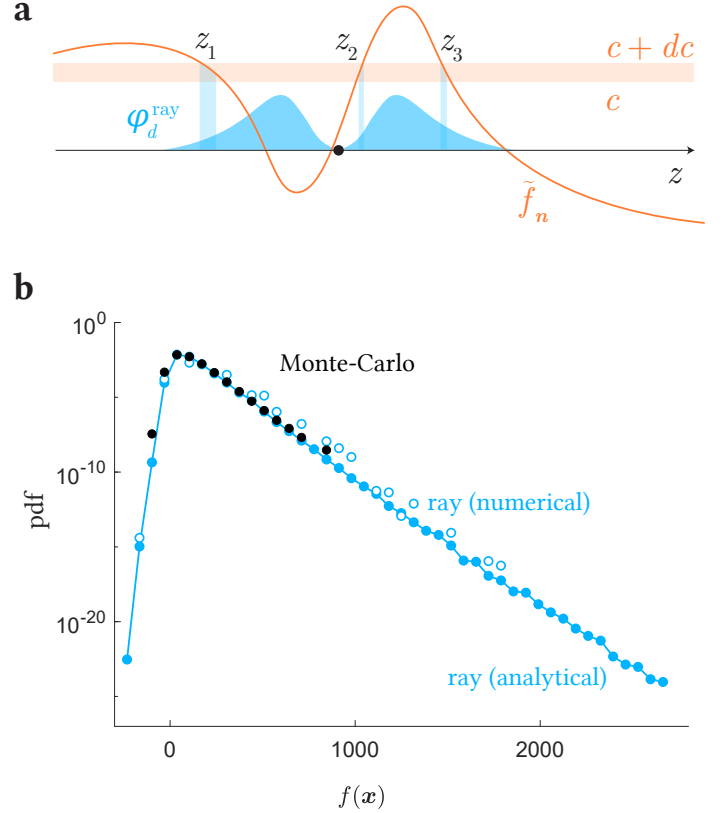


Figure 2: Ray-tracing method to compute the pdf of a general function $f(x)$ of a normal vector x . **a.** Schematic of the method. The arrow is a ray through the mean (dot) of a standard multinormal along n , and the blue pdf ϕ_d^{ray} is the standard multinormal density along the ray. $\tilde{f}_n(z)$ is the value of the standardized function $\tilde{f}(z)$ along the ray. The intervals where \tilde{f}_n lies between c and $c + dc$ are the blue widths at z_1 , z_2 and z_3 . **b.** The pdf of a cubic function of a 4-dimensional correlated normal vector, computed by three methods in the same computation time: Monte-Carlo sampling, vs. numerically differentiating the ray method cdf (open circles), vs. using the analytical derivative (filled circles). Missing dots are where a method wrongly computes the pdf as 0.

3.2 Computing the pdf

The ray-tracing method, which we developed to compute the cdf of any function $f(x)$ of a normal vector $x \sim N(\mu, \Sigma)$, can also be modified to compute the pdf. A simple way to compute the pdf at c is to compute the cdf at two nearby points $c \pm \Delta c$, and finite-difference them numerically. However, numerical differentiation is slower because it requires two evaluations of the cdf, and the differentiation itself introduces errors. We present here the calculations to do this differentiation analytically instead, which extends the ray-tracing method to be able to compute densities of arbitrary functions of normal random vectors with greater speed and accuracy.

In the ray method, we first linearly transform the space so that the multinormal becomes the standard normal z , and the function is transformed to the *standardized* function in this space: $\tilde{f}(z) = f(Sz + \mu)$, where $S = \Sigma^{\frac{1}{2}}$ is the symmetric square root. Similar to fig. 1 of our ray-tracing paper⁷ and corresponding explanations, fig. 2a here illustrates a ray sent from the origin (black dot) of the d -dimensional standard multinormal in the di-

rection of a unit vector \mathbf{n} . z is the coordinate along the ray, so that the vector location of point z on the ray is $\mathbf{z} = \mathbf{n}z$ in the full space. The blue distribution $\phi_d^{\text{ray}}(z) = f_{\chi_d}(|z|)/2$ (f_{χ_d} is the chi distribution pdf) is the density of the standard multinormal along the ray, and $\tilde{f}_{\mathbf{n}}(z)$ is the value of the function \tilde{f} along the ray.

Now, to find the pdf of $f(\mathbf{x})$ at c , we need to know the probability that $f(\mathbf{x})$, or $\tilde{f}(\mathbf{z})$ in the standardized space, is between c and $c + dc$. This is the probability that the $\tilde{f}_{\mathbf{n}}(z)$ along each ray \mathbf{n} is between c and $c + dc$, summed across all rays. Fig. 2a shows this horizontal slice. The probability that $\tilde{f}_{\mathbf{n}}(z)$ is within this slice is the probability of finding z within the corresponding vertical slices at z_1, z_2 or z_3 (the roots of $\tilde{f}_{\mathbf{n}}(z) - c$), given by $dp(\mathbf{n}) = \sum_i \phi_d^{\text{ray}}(z_i) |dz_i|$, where $|dz_i|$ is the width of each vertical slice, which can be found from the slope of the function: $|\tilde{f}'_{\mathbf{n}}(z_i)| = dc/|dz_i| \implies |dz_i| = dc/|\tilde{f}'_{\mathbf{n}}(z_i)|$. So we have $dp(\mathbf{n}) = \sum_i \phi_d^{\text{ray}}(z_i) / |\tilde{f}'_{\mathbf{n}}(z_i)| dc$. Now to integrate this across directions \mathbf{n} , we need to weight each $dp(\mathbf{n})$ by the volume fraction of the double-cone subtended by the differential angle element $d\mathbf{n}$, which is $\frac{2d\mathbf{n}}{\Omega_d}$ (Ω_d is the total angle in d dimensions), then sum. Since this gives us the probability that f is between c and $c + dc$, dividing away dc then gives us the probability density:

$$\frac{2}{\Omega_d} \int_{\Omega_d/2} \underbrace{\sum_i \frac{\phi_d^{\text{ray}}(z_i)}{|\tilde{f}'_{\mathbf{n}}(z_i)|}}_{\alpha(\mathbf{n})} d\mathbf{n}$$

For up to four dimensions, the integral is carried out numerically across half the total angle (since the probability on each ray already accounts for both directions of the ray). Beyond that, we perform a Monte Carlo integration, which finds the average value $\bar{\alpha}$ of the integrand over the *total* angle Ω_d , which is $\alpha(\mathbf{n})$ integrated over Ω_d , divided by Ω_d . Since the integral of $\alpha(\mathbf{n})$ over Ω_d is double that over $\Omega_d/2$, this automatically provides the extra factor of 2 needed to match the above equation.

Note that instead of inefficiently numerically computing the slope $\tilde{f}'_{\mathbf{n}}(z)$, we can see that it is simply the gradient of $\tilde{f}(\mathbf{z})$ in the direction \mathbf{n} : $\tilde{f}'_{\mathbf{n}} = \mathbf{n} \cdot \nabla \tilde{f}$. This still needs the gradient of the standardized function, but we can only expect the user to supply the gradient of the original function f . Fortunately, we can relate $\nabla \tilde{f}$ to ∇f . Remembering that $\tilde{f}(\mathbf{z}) = f(\mathbf{x})$, where $\mathbf{x} = \mathbf{S}\mathbf{z} + \boldsymbol{\mu}$, i.e. $x_j = \sum_i S_{ji} z_i + \mu_j$, we can write:

$$\begin{aligned} \nabla_i \tilde{f}(\mathbf{z}) &= \frac{\partial \tilde{f}(\mathbf{z})}{\partial z_i} = \frac{\partial f(\mathbf{x})}{\partial z_i} = \sum_j \frac{\partial f(\mathbf{x})}{\partial x_j} \frac{\partial x_j}{\partial z_i} \\ &= \sum_j \nabla_j f(\mathbf{x}) S_{ji} = \sum_j S'_{ij} \nabla_j f(\mathbf{x}). \end{aligned}$$

That is, $\nabla \tilde{f}(\mathbf{z}) = \mathbf{S}' \nabla f(\mathbf{S}\mathbf{z} + \boldsymbol{\mu})$. So, when f and ∇f are both supplied, the pdf can be computed more quickly and accurately. This method is available as function `norm_fun_pdf` in our toolbox 'Integrate and classify normal distributions' (source code on [github](#)).

Fig. 2b shows the pdf of a cubic function $f(\mathbf{x}) = x_1^3 + x_2^2 - x_3 x_4$ of a 4-dimensional normal:

$$\mathbf{x} \sim N(\boldsymbol{\mu}, \boldsymbol{\Sigma}), \quad \boldsymbol{\mu} = \begin{bmatrix} 4 \\ -2 \\ 3 \\ 2 \end{bmatrix}, \quad \boldsymbol{\Sigma} = \begin{bmatrix} 1 & 0 & -1 & 0 \\ 0 & 8 & 4 & 0 \\ -1 & 4 & 8 & 0 \\ 0 & 0 & 0 & 1 \end{bmatrix},$$

computed using three methods, using settings such that they take the same time. There exists no other standard specialized method for computing pdf's of general functions of multinormals, so our baseline reference is a Monte-Carlo method where we sample normal vectors, compute their function values, then histogram them to estimate the pdf. With 5 million samples, this takes 0.2s per point on an 8-core 3.9GHz Intel Xeon W-2245 CPU (all CPU computation times reported henceforth are on this), and reaches down to a value of only about 10^{-9} . The ray-tracing method with numerical differencing uses only 250 Monte-Carlo rays, and in the same time reaches down to about 10^{-17} , but is noisy due to numerical errors in the differencing. The analytical derivative method uses 1000 rays in the same time and reaches down to about 10^{-25} with greater precision. The remaining small noisy errors in the pdf are due to the Monte Carlo sampling of rays, and can be smoothed by growing the sample. Note the distinction from the vanilla Monte-Carlo method: in >4 dimensions the ray method uses Monte-Carlo integration, but only across rays at different angles (the radial integral is computed analytically), so it converges much faster than using vanilla Monte-Carlo integration over all dimensions, as in the baseline method here.

Suppose we are using this method to find the pdf of a generalized chi-square distribution at the point c . Then we first find the corresponding quadratic $q(\mathbf{z}) = \mathbf{z}' \mathbf{Q}_2 \mathbf{z} + \mathbf{q}'_1 \mathbf{z} + q_0$ of the standard (multi)normal. Then for any ray in this space in the direction \mathbf{n} , the value of this function is a quadratic of the z coordinate along the ray:⁷

$$\begin{aligned} q_{\mathbf{n}}(z) &= q(\mathbf{z}\mathbf{n}) = \mathbf{n}' \mathbf{Q}_2 \mathbf{n} z^2 + \mathbf{q}'_1 \mathbf{n} z + q_0 \\ &= q_2(\mathbf{n}) z^2 + q_1(\mathbf{n}) z + q_0. \end{aligned}$$

Now we find the roots of $q_{\mathbf{n}}(z) - c = q_2 z^2 + q_1 z + q_0 - c$. For there to exist two roots, we must have $q_2 \neq 0$ and the discriminant $\Delta = q_1^2 - 4q_2(q_0 - c) > 0$. Along the rays where this holds, the roots are $z_i = \frac{-q_1 \pm \sqrt{\Delta}}{2q_2}$, and the slope of the quadratic is the same magnitude at either root: $|q'(z_i)| = |2q_2 z_i + q_1| = \sqrt{\Delta}$. And if $q_2 = 0$ but $q_1 \neq 0$, then the function is a line with one root $z = \frac{c - q_0}{q_1}$, with slope magnitude $|q_1| = \sqrt{\Delta}$ again. These give us the quantities which we then integrate across different rays, either by quadrature (upto 4D) or Monte-Carlo, to get the generalized chi-square pdf at c . In our Matlab implementation `gx2pdf(..., 'method', 'ray')`, we implement this using fast vector operations, and speed up the Monte-Carlo integration by using the same sample of rays to compute the pdf at multiple points.

4 Inverse Fourier transform

4.1 Computing the cdf

Arguably the best existing general method to compute the generalized chi-square cdf $F(x)$ is Imhof's method,²² which uses the Gil-Pelaez theorem²³ to write it as an integral involving the characteristic function $\phi(t)$ (function `gx2char` in our toolbox):

$$F(x) = \frac{1}{2} - \frac{1}{\pi} \int_0^\infty \frac{\text{Im}[\phi(t) e^{-itx}]}{t} dt.$$

This integral is then carried out numerically to the requested tolerance, which sums the integrand over an adaptive grid to ap-

proximate the pdf at the single point x . However, let us follow a different path instead to get it to the form of a discrete inverse Fourier transform, starting from the Gil-Pelaez theorem:

$$\begin{aligned} F(x) &= \frac{1}{2} + \frac{1}{2\pi} \int_0^\infty \frac{\phi(-t) e^{itx} - \phi(t) e^{-itx}}{it} dt \\ &= \frac{1}{2} + \frac{1}{4\pi} \int_{-\infty}^\infty \frac{\phi(-t) e^{itx} - \phi(t) e^{-itx}}{it} dt \\ &= \frac{1}{2} + \frac{1}{2\pi} \int_{-\infty}^\infty \frac{\phi(-t)}{it} e^{itx} dt. \end{aligned}$$

This gets it into the form of a continuous inverse Fourier transform of the function $\tilde{\phi}(t) = \phi(-t)/it$. Now, suppose $t_n = n\Delta t$, $n = \{-N, \dots, N\}$ is a uniform grid from $-N\Delta t$ to $N\Delta t$, with spacing Δt . If $N\Delta t$ is large and Δt is small, then we can approximate the integral as a discrete sum:

$$F(x) \approx \frac{1}{2} + \frac{1}{2\pi} \sum_{n=-N}^N \tilde{\phi}(t_n) e^{it_n x} \Delta t.$$

Let's call $\tilde{\phi}_n = \tilde{\phi}(t_n)$. Now, suppose $x_j = j\Delta x$, $j = \{-N, \dots, N\}$ is a uniform grid of points. Substituting, we get:

$$F(x_j) \approx \frac{1}{2} + \frac{1}{2\pi} \sum_{n=-N}^N \tilde{\phi}_n e^{in\Delta t j\Delta x} \Delta t.$$

So if we select $\Delta t = \frac{2\pi}{(2N+1)\Delta x}$, this becomes:

$$F(x_j) \approx \frac{1}{2} + \frac{1}{\Delta x} \frac{1}{2N+1} \sum_{n=-N}^N \tilde{\phi}_n e^{2\pi i j n / (2N+1)} = \frac{1}{2} + \frac{\hat{\phi}_j}{\Delta x},$$

where $\hat{\phi}_j$ is the discrete inverse Fourier transform of $\tilde{\phi}_n$. Most programming languages have optimized IFFT functions, using which we can find a moderately accurate value of the cdf at not one, but simultaneously the entire grid of points, at blazing fast speeds. Increasing the range of the grid and reducing the spacing Δx improves accuracy, but sacrifices speed. There is another trade-off: the cdf is returned only over a uniform grid of points, whereas the Imhof-Davies method can compute it at any specific point. To do this here with IFFT, we first evaluate it over a fine grid that surrounds those points, then interpolate to the given points, which is still quite fast. This method is available as `gx2cdf(..., 'method', 'ifft')` in our toolbox.

4.2 Computing the pdf

The best existing method to compute the generalized chi-square pdf in general is also Imhof's method,²² which can be arrived at by differentiating the cdf expression, yielding:

$$f(x) = \frac{1}{\pi} \int_0^\infty \text{Re}[\phi(t) e^{-itx}] dt.$$

Similar to the case of the cdf, we shall instead try to change this to a discrete inverse Fourier transform, starting from the basic inversion formula:

$$f(x) = \frac{1}{2\pi} \int_{-\infty}^\infty \phi(t) e^{-itx} dt = \frac{1}{2\pi} \int_{-\infty}^\infty \phi(-t) e^{itx} dt.$$

This is a continuous inverse Fourier transform of the function $\tilde{\phi}(t) = \phi(-t)$. Following our previous derivation, we can approximate this as $f(x_j) \approx \frac{\hat{\phi}_j}{\Delta x}$, where $\hat{\phi}_j$ is the discrete inverse Fourier transform of $\tilde{\phi}_n = \tilde{\phi}(t_n)$. This method is available as `gx2pdf(..., 'method', 'ifft')` in our toolbox.

5 Finite-tail ellipse approximation

5.1 Computing the cdf

As we mentioned in the introduction, the generalized chi-square distribution has a finite tail when w_i are all the same sign and $s = 0$, i.e. when the quadratic is an ellipse. For example, consider all positive w_i and $s = m = 0$. The lower tail at 0 here is such a finite tail. Imhof's method is not very good at computing small cdf values in this tail, and as we discussed, neither is the ray method unless the components are all central. Ruben's method,²¹ which applies specifically to this situation, can be used to compute the cdf as a sum of chi-square cdf's:

$$F(x) = \sum_i a_i F_{\chi_{d+2i}^2}(x/\beta).$$

This method performs better in this tail and can reach down to `realmin` pretty fast, below which it returns 0. For the upper tail (complementary cdf), if we subtract the cdf from 1, it leaves a numerical residue and never gets smaller than about 10^{-16} . Instead, we can use a large number of terms in the Ruben series, and knowing that in this limit the a_i should sum to 1, we can write:

$$\bar{F}(x) = \sum_i a_i \bar{F}_{\chi_{d+2i}^2}(x/\beta).$$

This lets us go down to `realmin` in the upper tail as well.

We can also differentiate Ruben's method to obtain an expression for the pdf in this case as a sum of chi-square pdf's:

$$f(x) = \frac{1}{\beta} \sum_{i=0}^\infty a_i f_{\chi_{d+2i}^2}(x/\beta).$$

These are available as `gx2cdf(..., 'method', 'ruben')` and `gx2pdf(..., 'method', 'ruben')` in our Matlab toolbox.

Now in this section we show a simple approximation that can also be used for such a finite tail, which can reach much lower than Ruben's method and also becomes exact in that limit.

Note that in this case the quadratic form corresponding to the distribution is an ellipse (or an ellipsoid or hyper-ellipsoid in general), that gets vanishingly small as we approach the end of the tail, e.g. the purple ellipse in fig. 1c. The cdf is given by the probability inside this ellipse:

$$F(x) = p \left(\sum_{j=1}^d \omega_j (z_j - c_j)^2 < x \right).$$

The parameters of this ellipse can be easily identified once we write the quadratic form like in eq. 1. The ellipse is in $d = \sum k_i$ dimensions, and its center c is the vector built by appending each $\sqrt{\lambda_i}$ followed by a 0 $k_i - 1$ times. The weights ω_j are the elements

of the diagonal matrix \mathbf{Q}_2 derived in sec. 2, formed by appending each w_i k_i times. The semi-axis-lengths are $a_j = \sqrt{x/\omega_j}$.

A simple approximation for the probability inside this ellipse is to first compute the probability in the (hyper-) rectangle that encloses it (whose vertices are semi-axis-lengths above and below the center), using, say, Matlab's `mvncdf`, then multiplying it by the ratio of the ellipse volume to the rectangle volume. The approximation here is that we take the average probability density over the ellipse to be the same as over the rectangle, which becomes increasingly accurate as we approach the tail end and the ellipse gets tinier. However, computing the probability in the rectangle has its own associated error, and it cannot even always reach `realmin` like Ruben's fast exact method can, so this approximation is not very useful.

An even simpler approximation is to multiply the multinormal probability density at the ellipse center \mathbf{c} , with the ellipse volume:

$$\begin{aligned} \lim_{x \rightarrow 0} F(x) &= (2\pi)^{-\frac{d}{2}} e^{-\frac{\|\mathbf{c}\|^2}{2}} \frac{\pi^{\frac{d}{2}} \sqrt{\prod_j \frac{x}{\omega_j}}}{\Gamma(\frac{d}{2} + 1)} \\ &= \frac{(x/2)^{\frac{d}{2}} e^{-\frac{\|\mathbf{c}\|^2}{2}}}{\Gamma(\frac{d}{2} + 1) \sqrt{\prod_j \omega_j}}. \end{aligned} \quad (2)$$

So the cdf is simply proportional to a power of x . Here the approximation is that we take the average probability density over the ellipse to be the same as at its center, which again becomes more accurate as we approach the tail end.

This expression corresponds to the first term ($j = k = 0$) of the power series expression of $F(x)$ that Shah and Khatri³⁰ derived for this case, albeit not from a geometric interpretation such as this.

To better compute tiny cdf values at tiny x values, we can look at the log probability instead, which is simply linear in log x :

$$\begin{aligned} \lim_{x \rightarrow 0} \log_{10} F(x) &= \frac{d}{2} (\log_{10} x - \log_{10} 2) - \frac{\|\mathbf{c}\|^2}{\ln 100} \\ &\quad - \log_{10} \left[\Gamma\left(\frac{d}{2} + 1\right) \right] - \frac{1}{2} \sum_j \log_{10} \omega_j. \end{aligned}$$

This lets us directly compute the log of tiny tail probabilities given the log of tiny x values, all the way down to the absurdly small value of $\log_{10} F(x) = -\text{realmax} \approx -10^{308}$ (`realmax` is the largest double-precision number), i.e. $F(x) = 10^{-10^{308}}$, all in fast double precision.

We can also set lower and upper error bounds F_{\min} and F_{\max} for this cdf estimate, as the ellipse volume times the lowest and highest multinormal densities on the ellipse, i.e. at the points \mathbf{e}_f and \mathbf{e}_n on the ellipse that are farthest and nearest to the origin respectively. (The estimate is closer to the true value than this bound indicates, and even tighter bounds could be found, but this one is good enough as a first simple calculation.) When $\sum \lambda_i > 0$, i.e. the components are not all central, the ellipse is not at the origin, and these two points are where the line from the origin through the ellipse center intersects the ellipse. So they are equidistant from the ellipse center on opposite sides of it, of the form $\mathbf{c}(1 \pm r)$, and r is found by requiring that they satisfy the equation of the

ellipse:

$$\mathbf{e}_f, \mathbf{e}_n = \mathbf{c}(1 \pm r), \quad r = \sqrt{\frac{x}{\sum_j c_j^2 \omega_j}}.$$

Using these points we can express the bounds as fractions of the estimate itself:

$$\begin{aligned} \frac{F_{\min}}{F} &= e^{(\|\mathbf{c}\|^2 - \|\mathbf{e}_f\|^2)/2} = e^{-\|\mathbf{c}\|^2(r^2 + 2r)/2} \\ \Rightarrow \frac{\Delta F^-}{F} &= \frac{F - F_{\min}}{F} = 1 - e^{-\|\mathbf{c}\|^2(r^2 + 2r)/2}, \\ \text{similarly } \frac{\Delta F^+}{F} &= \frac{F_{\max} - F}{F} = e^{-\|\mathbf{c}\|^2(r^2 - 2r)/2} - 1. \end{aligned}$$

If these relative errors were constants, as we approach the tail end and the estimate goes to 0, the relative error would stay the same fraction of the estimate. But as $x \rightarrow 0$, $r \rightarrow 0$, and these estimation errors, even as a fraction of the estimate, go to 0 and the estimate becomes exact.

We can simplify the expressions for the relative errors at the limit, using the Maclaurin series of r and taking only up to the linear term, which gives us symmetric error bounds:

$$\lim_{x \rightarrow 0} \frac{\Delta F^-}{F} = \lim_{x \rightarrow 0} \frac{\Delta F^+}{F} = \|\mathbf{c}\|^2 r = \|\mathbf{c}\|^2 \sqrt{\frac{x}{\sum_j c_j^2 \omega_j}}.$$

We can again take the log of this to be able to compute small relative error bounds using the log of tiny x values.

Now, when each $\lambda_i = 0$, i.e. all the components are central, the ellipse is at the origin, and the points on the ellipse that are nearest and farthest from the origin are respectively its center, i.e. the origin itself, and the point at the tip of its longest axis, at a distance $\sqrt{x/\omega_{\min}}$. So if we use the density at the ellipse center for the cdf estimate, that is also its upper bound, and we can follow similar calculations as before to say that the lower relative error $\frac{\Delta F^-}{F} = 1 - e^{-x/2\omega_{\min}}$, and as $x \rightarrow 0$, this goes as $x/2\omega_{\min}$, so now it is proportional to x instead of \sqrt{x} and is tighter.

We can also invert the formula for the error to decide where we can reliably use the ellipse approximation. For a non-central ellipse, if we want a relative error of no more than δ , we can use the approximation in the range $x < \frac{\delta^2}{\|\mathbf{c}\|^4} \sum_j c_j^2 \omega_j$. For example, take $\mathbf{w} = [3 \ 1 \ 2]$, $\mathbf{k} = [4 \ 2 \ 3]$, $\boldsymbol{\lambda} = [7 \ 0 \ 2]$, $s = m = 0$. For a relative error of $< 1\%$, we can use the approximation for $x < 3 \times 10^{-5}$. For a central ellipse, we can use the approximation for $x < 2\delta\omega_{\min}$. For example, if all $\lambda_i = 0$ in this example, we can use the approximation for $x < 0.02$.

Fig. 3, left, compares the ellipse cdf estimate to Ruben's method for the above non-central parameters, in the range where the computed cdf is around `realmin`, so at some point Ruben's method falls to 0 and disappears in this plot. We compute the log of the Ruben cdf for this plot, and log becomes an erroneous operation at such low values, so the Ruben curve zig-zags before disappearing. For the ellipse estimate we can directly compute the log, and continue much further down without any numerical issues. The error-band shows 10^{35} times the error around the ellipse estimate, so the error is actually miniscule. The way we plotted these error-bands of $F \pm \alpha \Delta F$ ($\alpha = 10^{35}$) on a log axis is the following. Recall that the ellipse method returns the relative

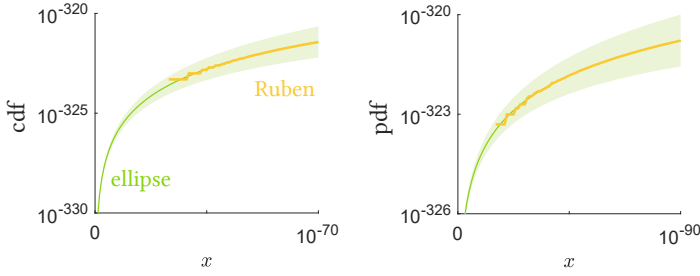


Figure 3: Comparing the ellipse approximation with Ruben’s method for computing the cdf (left) and pdf (right) in the finite tail. Error-bands represent 10^{35} times the error for the ellipse cdf estimate, and 10^{45} times the error for the ellipse pdf estimate.

estimation error δ . Then we can write:

$$\log_{10}(F \pm \alpha \Delta F) = \log_{10} F + \log_{10}(1 \pm \alpha \delta) \approx \log_{10} F \pm \frac{\alpha \delta}{\ln 10},$$

where in the second step we assume small δ , and have taken up to the linear term of its Maclaurin series.

In summary, we can see that the ellipse method agrees very well with Ruben’s method in this tail, and helps to extend it down to even smaller cdf values with tightening accuracy.

These results can be easily extended to the case of all-negative w_i , where the distribution is flipped and the upper tail is finite, and also when the offset is shifted to a non-zero m . This method is available as `gx2cdf(..., 'method', 'ellipse')` in our toolbox.

5.2 Computing the pdf

The ellipse approximation can also provide an expression for the pdf in the finite tail, by simply differentiating the cdf, eq. 2, w.r.t. x :

$$\lim_{x \rightarrow 0} f(x) = \frac{x^{\frac{d}{2}-1} d e^{-\frac{\|c\|^2}{2}}}{2^{\frac{d}{2}+1} \Gamma\left(\frac{d}{2} + 1\right) \sqrt{\prod_j \omega_j}}. \quad (3)$$

We can again take the log of this to be able to compute the log of tiny density values at tiny x values, down to $f(x) = 10^{-10^{308}}$. We can also set error bounds here again. The pdf approximation can be thought of as the rate of change of the ellipse volume with x , multiplied with the density at the ellipse center. As before, to get the error bounds we can instead multiply with the densities at the ellipse points closest and farthest from the origin. This leads to the same relative errors as for the cdf, for both the non-central and central cases.

This method is available as `gx2pdf(..., 'method', 'ellipse')` in our toolbox.

Fig. 3, right, compares the pdf computed by the ellipse method and Ruben’s method (which is the best pdf method for the finite tail), for the same parameters again. The error-band here shows 10^{45} times the error of the ellipse method, so it is again tiny. So for the pdf too, the ellipse method agrees well with Ruben’s method and extends it much farther into the tail.

6 Comparing the methods

6.1 Computing the cdf

In fig. 4a, we compute the cdf of a generalized chi-square with $w = [2 \ 4 \ .5]$, $k = [3 \ 5 \ 1]$, $\lambda = [4 \ 1 \ .3]$, $s = m = 0$, which has a lower finite tail and an upper infinite tail. We use Imhof’s method (with double precision for the middle and variable precision in the tails, and a relative error tolerance of 10^{-10}), IFFT (with a grid of $N = 10^7$ points that spans the region plotted), ray-tracing (with 10^6 rays and double precision in the lower tail, and 100 rays and variable precision in the upper), Ruben’s method (with 100 terms in the lower tail and 10^4 in the upper), and the ellipse approximation (only in the lower tail).

To clearly show both the center and the tails of the distribution in the same plot, we have used a few plotting tricks. First, we plot the lower tail probability (cdf) until the median (cdf=0.5), and the upper tail probability (complementary cdf) beyond it, so that we can show both tails on the same vertical log axes. Second, we select the main body of the distribution here to be the region above a lower or upper tail probability of 0.001 (area highlighted purple). We use linear horizontal and vertical axes to show this area clearly, but in the tails we use log horizontal and vertical axes (areas highlighted red). Missing dots are where a method wrongly computes a small tail probability as 0, so it cannot be shown on a log axis.

We see that in the center of the distribution, all the exact methods agree well. In the finite lower tail, Imhof’s method reaches accurately down to about 10^{-6} , beyond which it returns incorrect values, sometimes negative, which we clip to 0, so those points are missing on this log plot (while discussing fig. 4b we shall elaborate on this limitation). The IFFT method with its settings here levels out at around 10^{-5} , so it is not very accurate without sacrificing much more in terms of speed. The ray-trace method with double precision stops at 10^{-6} and returns 0 below that, due to the reason of the vanishing ellipsoidal integration domain we described in sec. 3.1. This limits the ray method in this finite tail well before `realmin`, and variable precision does not even kick in. Ruben’s method computes accurately down to about `realmin`, and the ellipse method can compute accurately all the way down to $10^{-10^{308}}$, which we don’t show here. In the infinite upper tail, Imhof’s method returns incorrect values below 10^{-15} , even with variable precision, and IFFT again flattens out at 10^{-5} . Ruben’s method can again reach `realmin` here. Ray-trace with double precision can also reach `realmin`, beyond which it uses variable precision to continue for *hundreds of millions* more orders of magnitude to `symmin`, which is so far down that we have breaks in the vertical and horizontal axes to show it in the same plot.

In the table below the figure, we list the smallest upper and lower tail probabilities that could be reached using these methods with these settings, along with the computation speeds. Ray-trace can also use an onboard GPU (here the NVIDIA GeForce RTX 3070), but only with double precision, and can be about 4 times faster than the CPU, but only when using at least about 10^6 rays, due to overhead. With variable precision on the CPU, it takes the same time regardless of how small the output is, all the way down to `symmin`.

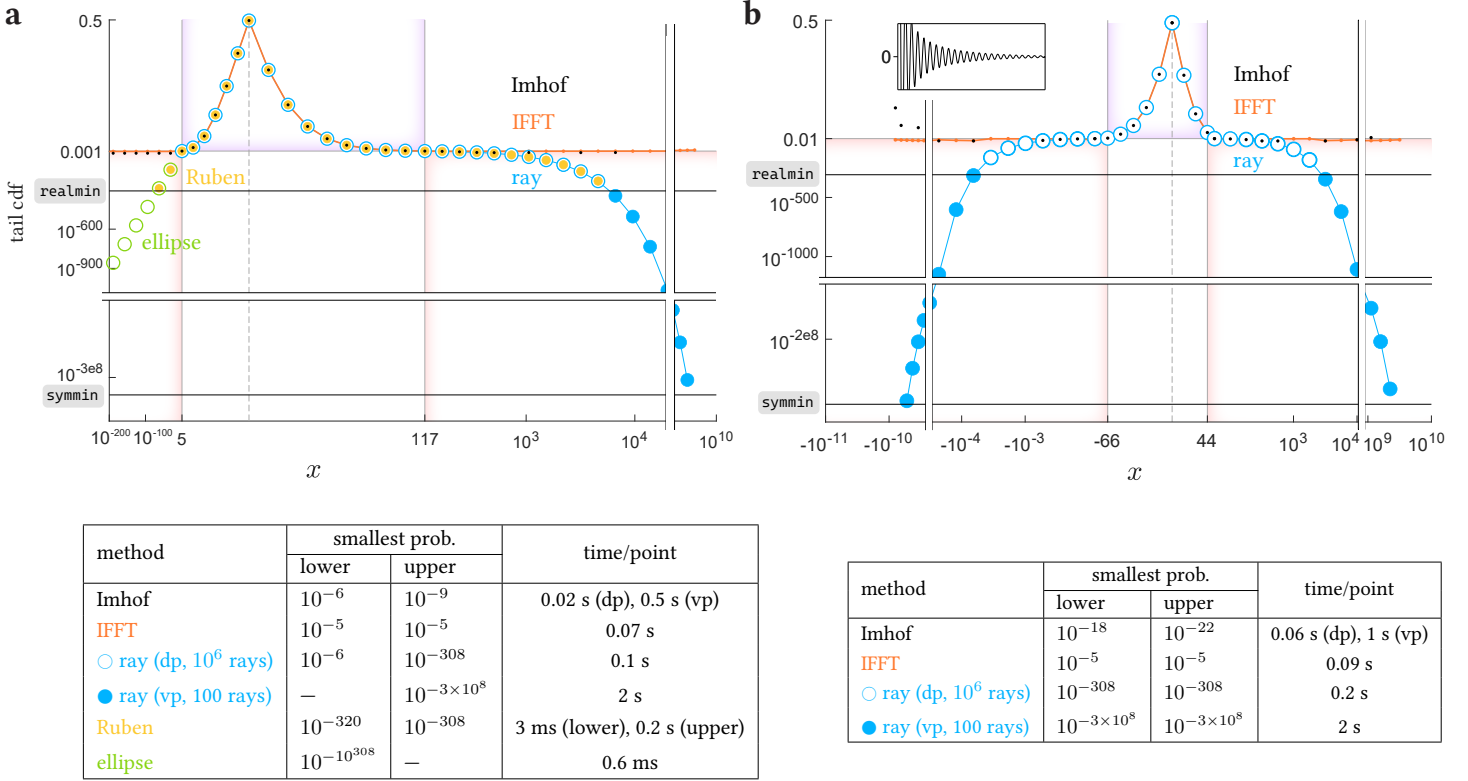


Figure 4: Computing the generalized chi-square cdf. **a.** Cdf of a generalized chi-square with a lower finite and upper infinite tail, computed with Imhof, IFFT, Ruben, ellipse, and ray-trace with double precision (open circles) and variable precision (filled). We plot the lower tail probability (cdf) till the median (dashed vertical line), and upper tail probability (complementary cdf) beyond it. The middle of the distribution, probabilities >0.001 (area highlighted purple) is in linear axes, and the tail regions (areas highlighted red) are in double log axes. The vertical and horizontal white stripes are breaks in the axes, to be able to show the end of the upper tail in the bottom-right, which is much farther below. `realmin` = 10^{-308} is the double-precision limit, and `symmin` $\approx 10^{-3 \times 10^8}$ is the variable-precision limit. Any missing dots are where a method wrongly computes the tail probability as 0. The table below shows the rough orders of the smallest lower (finite) and upper (infinite) tail probabilities reached by the different methods with their respective settings, and their computation times per point. ‘dp’ and ‘vp’ mean double and variable precision. **b.** Cdf of a generalized chi-square with two infinite tails computed with the methods. Middle area of probability >0.01 is in linear axes, tail areas are in log axes. Inset: Imhof integrand at $x = -2000$. Similar table below of smallest probabilities and speeds.

In summary, all the exact methods are good for the middle of this elliptical distribution. Only Ruben and the ellipse approximation are good for the far lower finite tail, and in the far upper infinite tail, ray-trace is the best.

We can also use our methods to compute the cdf of a non-central chi-square, which is a special case of the generalized chi-square, see supp. fig. S1. Matlab’s `ncx2cdf` implements a fast and relatively straightforward calculation for this special case, and can reach down to `realmin` in its finite lower tail, where the ray method again stops short due to the vanishing domain. But in the infinite upper tail, `ncx2cdf` stops at 10^{-18} , whereas ray-trace reaches `realmin` with double precision and `symmin` with variable precision. In summary, for non-central chi-square cdf’s, `ncx2cdf` is the best method for the lower tail and center, but in the upper tail the ray method is best.

In fig. 4b we compute probabilities of a generalized chi-square with $w = [1 \ -5 \ 2]$, $k = [1 \ 2 \ 3]$, $\lambda = [2 \ 3 \ 7]$, $s = 10$ and $m = 5$, which has two infinite tails. We use Imhof, IFFT and the ray-trace methods with the same settings as before. In the center of the distribution the methods again agree well. But in the tails, the Imhof method again computes small probabilities inaccurately, and they are sometimes negative (which we clip to

0 and these are the missing black dots). This is because in the tail, the Imhof integrand related to the characteristic function (see inset) is highly oscillatory and integrates to a tiny probability. So when numerically integrated, the larger oscillations must be computed to precisely cancel and accurately produce the tiny residual sum. When this does not work so precisely, the integral is either above or below the true value. The ray method is an entirely different approach where the contribution to the integral from each ray is non-negative, and they never cancel each other. So it avoids this problem and can again reach down to `realmin` quite fast with double precision, and then to `symmin` with variable precision, while still matching Imhof in speed. It works well in both tails here because they are both infinite. The IFFT method is fast, but less capable of accurately reaching such small tail probabilities. The table below the figure lists the smallest tail probabilities that could be reached by these methods with these settings, along with their speeds.

To compute the inverse cdf, our `gx2inv` function uses numerical root-finding on the forward cdf function, which can automatically pick the best cdf method given the distribution parameters. Since the ray method can compute such small probabilities in an infinite tail, `gx2inv` can leverage this to find quantiles cor-

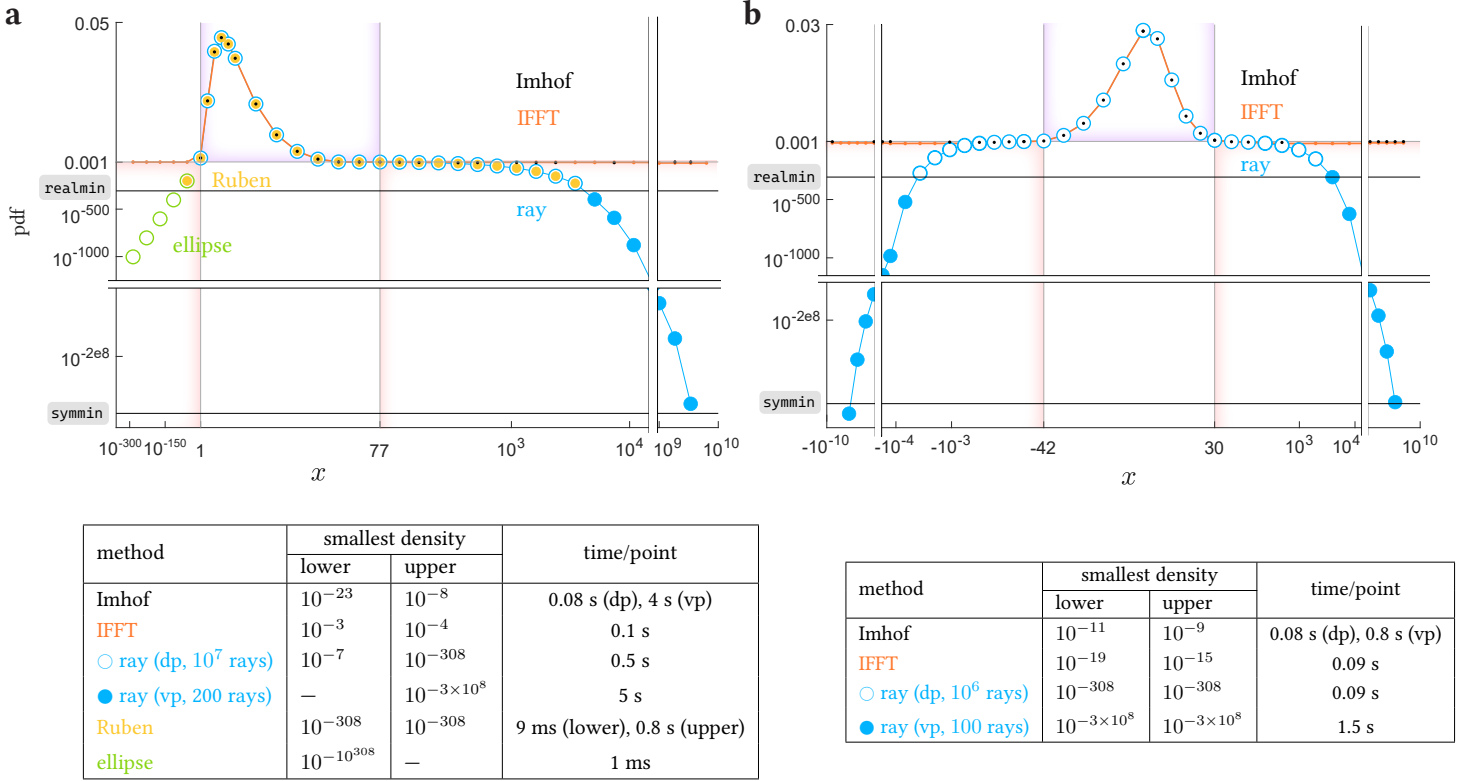


Figure 5: Computing the generalized chi-square pdf. **a.** Pdf of a generalized chi-square with a lower finite and upper infinite tail, computed with Imhof, IFFT, Ruben, ellipse, and ray-trace with double precision (open circles) and variable precision (filled). The middle of the distribution, probabilities >0.001 (area highlighted purple) is in linear axes, and the tail regions (areas highlighted red) are in double log axes. The vertical and horizontal white stripes are breaks in the axes, to be able to show the end of the upper tail in the bottom-right, which is much farther below. The table below shows the rough orders of the smallest densities computed accurately in the lower (finite) and upper (infinite) tails here by the different methods, and their computation times per point. **b.** Pdf of a generalized chi-square with two infinite tails computed with the methods. Middle area of probability >0.001 is in linear axes, tail areas are in log axes. Similar table below of smallest densities and speeds.

responding to probabilities in an infinite tail that are as small as `symmin`, which is not possible by inverting other cdf methods.

6.2 Computing the pdf

In fig. 5a, we compute the pdf of a generalized chi-square with $\mathbf{w} = [1 \ 3 \ .5 \ .2]$, $\mathbf{k} = [3 \ 1 \ 2 \ 1]$, $\boldsymbol{\lambda} = [0 \ 3 \ 5 \ 0]$, $s = m = 0$, which has a lower finite tail and an upper infinite tail. We use Imhof’s method (with variable precision in the lower tail and double precision for the rest, and a relative error tolerance of 10^{-10}), IFFT (with a grid of $N = 10^7$ points that spans the region plotted), ray-tracing (with 10^7 rays and double precision in the lower tail and body, and 200 rays and variable precision in the upper tail), Ruben’s method (with 100 terms in the lower part and 10^4 in the upper part), and the ellipse approximation (only in the lower tail).

We see again that in the center of the distribution, all the exact pdf methods agree well. In the finite lower tail here, Imhof’s method reaches accurately down to about 10^{-23} , IFFT levels out at 10^{-3} , and ray-tracing with double precision stops at 10^{-7} (variable precision does not help). Ruben’s method reaches accurately down to about `realmin`, and the ellipse method can again compute accurately until $10^{-10^{308}}$, which we don’t show here. In the infinite upper tail, Imhof’s method reaches about 10^{-8} , IFFT flattens out at 10^{-4} , and Ruben’s method can again reach `realmin`.

Ray-trace with double precision can also reach `realmin`, beyond which it uses variable precision to continue until `symmin`.

In the table below the figure, we list the smallest probability densities computed correctly in the lower and upper tails using these methods with their settings, along with their computation speeds.

In fig. 5b we compute probabilities of a generalized chi-square with $\mathbf{w} = [4 \ -1 \ 2 \ -3]$, $\mathbf{k} = [1 \ 1 \ 2 \ 3]$, $\boldsymbol{\lambda} = [0 \ 4 \ 0 \ 2]$, $s = 3$ and $m = 10$, which has two infinite tails. We use Imhof’s method (with double precision and relative tolerance of 10^{-10}), IFFT (with the same settings as before), and ray-trace (with 10^6 rays and double precision in the body, and 100 rays and variable precision in the tails). In the center of the distribution the methods again agree well. But in the tails, Imhof and IFFT stop early, whereas the ray method can again reach down to `realmin` quite fast with double precision, and then to `symmin` with variable precision with reasonable speed.

In summary, just like for the cdf, all the exact pdf methods work well in the middle of the distributions. The ray method works well in the infinite tails in all cases, and only Ruben and the ellipse approximation work in the finite tail.

Based on our comparisons, we list in table 1 the cdf and pdf methods discussed in this paper that work the best in different parts of a generalized chi-square distribution in different cases.

$\tilde{\chi}$ type	part	best cdf/pdf method(s)
ellipse: w_i same sign, $s = 0$	body	Ruben, Imhof, IFFT, ray
	finite tail	Ruben, ray (if $\lambda_i = 0$), ellipse
	infinite tail	Ruben, ray
not ellipse: w_i mixed signs, and/or $s \neq 0$	body	Imhof, IFFT, ray
	infinite tails	ray
sphere: non-central χ^2 (only one term)	body	<code>ncx2cdf</code>
	finite tail	<code>ncx2cdf</code> , ellipse
	infinite tail	ray

Table 1: The best cdf and pdf methods to use for the different parts of the generalized chi-square distribution in different cases.

7 More accuracy tests

7.1 Against published tables

Imhof²² provides a table that lists some upper tail cdf values of some generalized chi-square distributions with mixed-sign weights (but with $s = m = 0$). In table 2, nos. 1-12, we list those ‘exact’ values. No information is provided about their accuracy, so we assume that they are rounded to four places, i.e. their uncertainty is ± 0.5 in the last digit. Liu et al²⁶ also provide a table that lists some upper tail cdf values of some generalized chi-square distributions with only positive weights (i.e. these are all infinite tails), computed with Ruben’s exact method to a greater precision of 6 digits (nos. 13-16 here). We compare the outputs from our implementations of the exact methods, i.e. Imhof, ray-trace and IFFT, against these exact values, using roughly the minimum settings needed to reach this precision.

Up to 4 total degrees of freedom, the ray method can be used with adaptive grid integral (quadrature), to the error tolerance that we specify. Beyond this it performs slower Monte-Carlo integration (on the GPU here), and reports the standard error of the output, and we increase the number of Monte-Carlo rays (mentioned in the table) until we reach the required precision. The IFFT method does not report uncertainty values, but we increase its grid span and number of grid points N (mentioned in the table) until its output converges to the desired precision.

We see that in almost all cases, all our values match each other and the exact values within uncertainty. (If two numbers are $p_1 \pm \Delta p_1$ and $p_2 \pm \Delta p_2$, they agree if $|p_1 - p_2| \leq \Delta p_1 + \Delta p_2$.) In two cases, Imhof’s published exact values deviate slightly from the uncertainty range of our values (including our implementation of Imhof’s method itself), and we believe that our values are more correct, since we compute them to greater precision and they match each other.

Imhof’s method is by far the fastest here for the same accuracy, and therefore the best. This is for two reasons. First, here we compute values over only three points, whereas ray-trace and IFFT use vector operations that are faster when simultaneously computing values over many points. Second, these values were not too far in the tails and only had up to 6 decimal places, but when we are far in the tails or need much more accuracy, the

Imhof integral slows down or quits with a wrong value, unlike ray-trace.

7.2 With randomly sampled parameters

Bodenham et al²⁹ have suggested that testing the accuracy of methods on a few points across some hand-picked distributions, as in the previous section, is not thorough enough, and instead recommend to randomly sample a large set of generalized chi-square parameters, then compare the methods across an array of quantile points for each distribution in the set. In this section we show performance tests along these lines.

We first randomly sample a broad set of parameters. We draw the number n of constituent non-central chi-square terms uniformly from 1 through 10. Then we draw each of the n weights w_i from a standard normal distribution, and each of the n degrees of freedom k_i uniformly from 1 through 10. Each non-centrality λ_i is with equal probability either 0 (so that term is a central chi-square), or equal to 10^z , where z is a standard normal, so that the non-centrality can spread across several orders of magnitude. Similarly, s is with equal probability either 0 (so that there is no linear term), or equal to 10^z . m is also drawn similarly to s , except that its sign is positive or negative with equal probability.

With this sampling, almost all distributions generated are non-elliptical, i.e. with both tails infinite. We keep 2000 of these non-elliptical distributions, then we separately generate 2000 elliptical distributions with a lower finite tail, by keeping s at 0, and taking the absolute values of the w_i . This allows us to test our methods equally over both elliptical and non-elliptical distributions.

Now we select an array of 19 quantile values p_q : these are 10 lower tail probability (cdf) values uniformly logarithmically spaced from 10^{-10} to 0.5 (the median), then upper tail probability (complementary cdf) values similarly arrayed from the median to 10^{-10} . Now, for each of our 4000 distributions, we use our `gx2inv` function to find the quantile points corresponding to these probabilities p_q . `gx2inv` uses numerical root-finding to invert the `gx2cdf` function, whose cdf method is automatically selected based on the parameters, so for elliptical and non-elliptical distributions, it inverts Ruben’s method and Imhof’s method respectively. In fig. 6a we first look at the accuracy of this inverse cdf function, by plotting the relative discrepancy between the desired quantile value p_q , and the true tail probability p computed by Ruben’s or Imhof’s method at the inverted quantile point: $|(\log_{10} p - \log_{10} p_q) / \log_{10} p_q|$. We measure the discrepancy in the order of the probability instead of the probability itself, because p_q is arrayed across several scales, and we find that the discrepancies in the order of magnitude, and not the value itself, are what is more comparable across these different scales. If p at the inverted quantile was wrongly computed as 0, we take the relative discrepancy to be 1.

Not surprisingly, we see that for the same settings, the inversion starts to become more erroneous in the tails. When inverting Imhof’s method for non-elliptical distributions with both infinite tails, this rise in error is more symmetric, but when inverting Ruben’s method for elliptical distributions, the error is much lower for the upper infinite tail than the lower finite tail.

At each of these quantile points, we now compute the tail probability and density with high accuracy, so that we have reliable

#	$\tilde{\chi}$ parameters	x	exact value	Imhof		ray-trace		IFFT	
				value	time	value	time	value	time
1	$w = [.6 \ .3 \ .1]$ $k = [1 \ 1 \ 1]$ $\lambda = [0 \ 0 \ 0]$.1	.9458	.9458(1)	0.04 s	.9458(1)	3.5 s GPU, MC w 10^7 rays	.9458	0.1 s span = 10^4 , $N = 10^6$
		.7	.5064	.5064(1)		.5064(1)		.5064	
		2	.1240	.1240(1)		.1240(1)		.1240	
2	$w = [.6 \ .3 \ .1]$ $k = [2 \ 2 \ 2]$ $\lambda = [0 \ 0 \ 0]$.2	.9936	.993547(1)	0.03 s	.993545(5)	3.5 s GPU, MC w 10^7 rays	.993546	9.5 s span = 10^6 , $N = 10^8$
		2	.3998	.399795(1)		.3997(1)		.3998	
		6	.0161	.016103(1)		.01610(1)		.0161	
3	$w = [.6 \ .3 \ .1]$ $k = [6 \ 4 \ 2]$ $\lambda = [0 \ 0 \ 0]$	1	.9973	.9973(1)	0.01 s	.997319(3)	4.7 s GPU, MC w 10^7 rays	.9973	0.1 s span = 10^5 , $N = 10^6$
		5	.4353	.4353(1)		.4353(1)		.4353	
		12	.0088	.0088(1)		.008770(7)		.0088	
4	$w = [.6 \ .3 \ .1]$ $k = [2 \ 4 \ 6]$ $\lambda = [0 \ 0 \ 0]$	1	.9666	.9666(1)	8 ms	.96665(3)	4.8 s GPU, MC w 10^7 rays	.9666	0.08 s span = 10^5 , $N = 10^6$
		3	.4196	.4196(1)		.4196(1)		.4196	
		8	.0087	.00871(1)		.00871(1)		.0087	
5	$w = [.7 \ .3]$ $k = [6 \ 2]$ $\lambda = [6 \ 2]$	2	.9939	.9939(1)	7 ms	.99391(9)	1 s GPU, MC w 10^6 rays	.9939	1 s span = 10^6 , $N = 10^7$
		10	.4087	.4087(1)		.4087(2)		.4087	
		20	.0221	.0221(1)		.02210(6)		.0221	
6	$w = [.7 \ .3]$ $k = [1 \ 1]$ $\lambda = [6 \ 2]$	1	.9549	.9549(1)	0.01 s	.9548(1)	0.1 s grid integral	.9549	1 s span = 10^6 , $N = 10^7$
		6	.4076	.4076(1)		.4076(1)		.4076	
		15	.0223	.0223(1)		.0223(1)		.0223	
7	$w = [.2 \ .1 \ \frac{1}{3} \ .4 \ \frac{2}{3}]$ $k = [10 \ 4 \ 2 \ 2 \ 6]$ $\lambda = [0 \ 0 \ 0 \ 0 \ 0]$	1.5	.9891	.9891(1)	0.01 s	.98906(1)	8.4 s GPU, MC w 10^7 rays	.9891	2.5 s span = 2×10^5 , $N = 2 \times 10^7$
		4	.3453	.3453(1)		.3453(1)		.3453	
		7	.0154	.0154(1)		.01541(2)		.0154	
8	$w = [.2 \ .1 \ \frac{1}{3} \ -.4 \ -.2 \ -\frac{2}{3}]$ $k = [6 \ 4 \ 2 \ 2 \ 4 \ 6]$ $\lambda = [0 \ 0 \ 0 \ 0 \ 0 \ 0]$	-2	.9102	.910225(1)	.01 s	.91024(4)	2.8 m GPU, MC w 2×10^8 rays	.9102	14 s span = 10^6 , $N = 10^8$
		0	.4061	.406106(1)		.40609(9)		.4061	
		2.5	.0097	.009760(1)		.009758(7)		.00976	
9	$w = [\frac{7}{2} \ \frac{3}{2}]$ $k = [7 \ 3]$ $\lambda = [12 \ 4]$	3.5	.9563	.9563(1)	7 ms	.9564(2)	0.7 s GPU, MC w 10^6 rays	.9563	9.5 s span = 10^6 , $N = 10^8$
		8	.4152	.4152(1)		.4152(1)		.4152	
		13	.0462	.0462(1)		.0463(1)		.0462	
10	$w = [\frac{7}{2} \ \frac{3}{2} \ -\frac{7}{2} \ -\frac{3}{2}]$ $k = [6 \ 2 \ 1 \ 1]$ $\lambda = [6 \ 2 \ 6 \ 2]$	3.5	.9218	.9218(1)	9 ms	.9215(3)	0.8 s GPU, MC w 10^6 rays	.9218	1.2 s span = 10^6 , $N = 10^7$
		8	.4779	.4779(1)		.4780(2)		.4779	
		13	.0396	.0396(1)		.0397(1)		.0396	
11	$w = [\frac{4}{4} \ \frac{3}{4} \ \frac{1}{4} \ \frac{7}{4}]$ $k = [8 \ 11 \ 8 \ 7]$ $\lambda = [0 \ 4 \ 0 \ 12]$	3	.9842	.9842(1)	6 ms	.9842(1)	1.1 s GPU, MC w 10^6 rays	.9842	1.3 s span = 10^6 , $N = 10^7$
		6	.4264	.4264(1)		.4263(3)		.4264	
		10	.0117	.0117(1)		.01165(6)		.0117	
12	$w = [.1 \ \frac{1}{2} \ \frac{1}{6} \ -\frac{7}{6} \ -\frac{1}{2} \ \frac{7}{3} \ -.2 \ -.1 \ -\frac{1}{3}]$ $k = [7 \ 4 \ 2 \ 6 \ 2 \ 1 \ 2 \ 4 \ 6]$ $\lambda = [2 \ 0 \ 0 \ 6 \ 2 \ 6 \ 0 \ 0 \ 0]$	-3	.9861	.9861(1)	8 ms	.9862(1)	1.1 s GPU, MC w 10^6 rays	.9861	0.1 s span = 10^5 , $N = 10^6$
		0	.5170	.5170(1)		.5170(5)		.5170	
		4	.0152	.0152(1)		.0152(1)		.0152	
13	$w = [.5 \ .4 \ .1]$ $k = [1 \ 2 \ 1]$ $\lambda = [1 \ .6 \ .8]$	2	.457461(1)	.457461(1)	0.02 s	.457461(1)	2.5 s grid integral	.457460	33 s span = 4×10^6 , $N = 2 \times 10^8$
		6	.031109(1)	.031109(1)		.031109(1)		.031109	
		8	.006885(1)	.006885(1)		.006885(1)		.006886	
14	$w = [.7 \ .3]$ $k = [1 \ 1]$ $\lambda = [6 \ 2]$	1	.954873(1)	.954873(1)	0.09 s	.954873(1)	0.3 s grid integral	.954872	31 s span = 4×10^6 , $N = 2 \times 10^8$
		6	.407565(1)	.407565(1)		.407565(1)		.407565	
		15	.022343(1)	.022343(1)		.022343(1)		.022344	
15	$w = [.995 \ .005]$ $k = [1 \ 2]$ $\lambda = [1 \ 1]$	2	.347939(1)	.347939(1)	0.2 s	.347939(1)	0.4 s grid integral	.347938	1.3 m span = 4×10^6 , $N = 10^9$
		8	.033475(1)	.033475(1)		.033475(1)		.033476	
		12	.006748(1)	.006748(1)		.006748(1)		.006749	
16	$w = [.35 \ .15 \ .35 \ .15]$ $k = [1 \ 1 \ 6 \ 2]$ $\lambda = [6 \ 2 \ 6 \ 2]$	3.5	.956318(1)	.956318(1)	7 ms	.956322(8)	7 m GPU, MC w 10^9 rays	.956318	2.8 m span = 10^7 , $N = 10^9$
		8	.415239(1)	.415239(1)		.415234(5)		.415239	
		13	.046231(1)	.046231(1)		.046230(4)		.046231	

Table 2: Testing the accuracy of computing the generalized chi-square upper-tail cdf (probability that $\tilde{\chi}$ exceeds x) with our implementations of Imhof, ray-trace and IFFT methods, against previously published exact values in Imhof’s table²² (nos. 1-12, which have mixed-sign weights, and which we assume are rounded to 4 places, i.e. have an uncertainty of ± 0.5 in the last digit), and Liu et al’s table²⁶ (nos. 13-16, which have all positive weights, computed with Ruben’s method²¹ to 6 digits). In all cases, the parameters $s = m = 0$. Digits in parentheses at the end signify uncertainty, eg (1) means ± 1 in the last digit. IFFT does not return uncertainty, and its values are rounded to the last digit. In each row, all green values match each other within uncertainty. Our methods are used with roughly the minimum settings needed to reach the required precision. Reported times are to compute all three cdf values of a distribution. ‘MC’ means Monte-Carlo integration.

ground-truth values: we use Ruben’s method (with 1000 terms) and Imhof’s method (with variable precision and a small relative error tolerance of 10^{-15}) for the elliptical and non-elliptical distributions respectively. Ruben takes an avg. \pm sd of 0.5 ± 0.1 s to compute all 19 cdf values of a distribution, and Imhof takes 8 ± 5 s. We then compute those cdf and pdf values using the ray and IFFT methods. The lower tail probabilities and densities here in the elliptical distributions are not small enough to use the ellipse approximation. We use ray with double precision, and 2×10^6

rays for the cdf and 10^7 rays for the pdf, and IFFT with a span of 10^5 times the range from the lowest to the highest quantile, and 2×10^7 grid points for the cdf, and a span of 4×10^5 times that range, and 10^8 grid points for the pdf. These settings were selected roughly via trial and error on a few distributions, and are not sacrosanct, and with these settings ray and IFFT need roughly equal time. For computing all 19 cdf values for each distribution, ray took an avg. \pm sd of 6 ± 1 s, and IFFT took 5 ± 1 s. For computing all the pdf values for each distribution, ray took 12 ± 3 s,

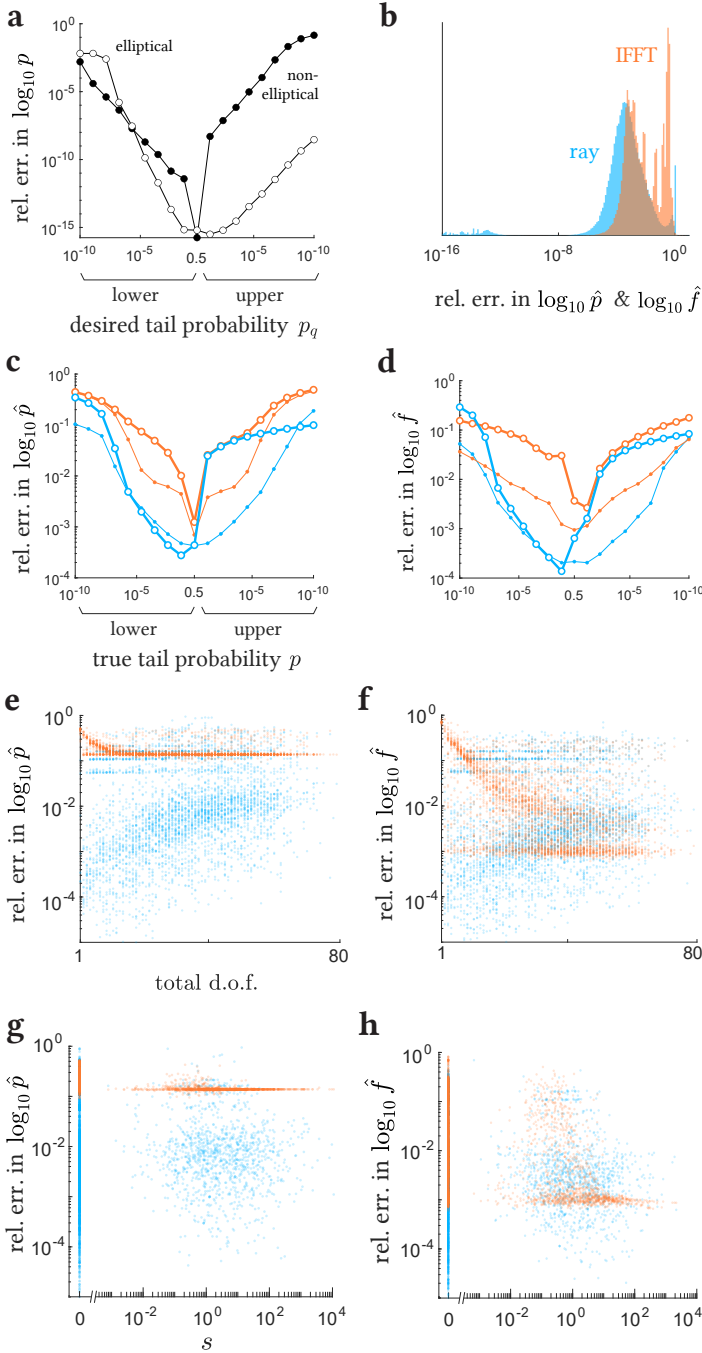


Figure 6: Computation errors in our methods across randomly-sampled distributions. **a:** Avg. relative discrepancy between the desired tail probability p_q and the actual tail probability p at each inverted quantile, for elliptical and non-elliptical distributions. **b:** Distribution of relative errors of the orders of the tail cdf \hat{p} and pdf \hat{f} estimated by the ray and IFFT methods, against Ruben and Imhof method estimates. **c-d:** Relative errors in estimating the tail cdf and the pdf, against an array of quantile points. Open and filled circles are for elliptical and non-elliptical distributions resp. **e-f:** Relative errors of cdf and pdf estimates against the total degrees of freedom of each distribution. **g-h:** Relative errors of cdf and pdf estimates against the value of s of each distribution. The vertical stack on the left is for $s = 0$.

and IFFT took 15 ± 3 s.

We then compute the fractional error in estimating the or-

der of magnitude of the probability and density: $|(\log_{10} \hat{p} - \log_{10} p) / \log_{10} p|$ and $|(\log_{10} \hat{f} - \log_{10} f) / \log_{10} f|$, where p and f are respectively the tail probability (cdf below median, and complementary cdf above median) and density computed by the ground-truth (Ruben or Imhof) method, and \hat{p} and \hat{f} are computed by ray and IFFT. If \hat{p} or \hat{f} was wrongly computed as 0, we again take the relative error to be 1. For a small fraction of cases, the ground-truth p or f was also wrongly computed as 0, and we omit these cases.

Across all 19 quantiles of the elliptical distributions with a finite tail, the average \pm sd of the relative error of estimating the log tail probability was 0.03 ± 0.49 with the ray method, and 0.14 ± 0.17 by the IFFT method. On the non-elliptical distributions with two infinite tails, the relative estimation error was 0.07 ± 0.23 by the ray method, and 0.18 ± 0.20 by IFFT. So the ray method is better on average for the same computation time. The relative error of estimating the log probability density on the elliptical distributions was 0.05 ± 0.19 with the ray method, and 0.08 ± 0.22 with IFFT, and on the non-elliptical distributions it was 0.01 ± 0.12 with the ray method, and 0.01 ± 0.07 with IFFT. So for computing the density, ray and IFFT are on average equally accurate for the same time. Fig. 6b shows the overall distributions of these relative estimation errors of the log probability and density across all the distributions. We see that the ray method is overall more accurate for the same computation time.

Now we look at the variation in the cdf and pdf accuracy across different parameters. Figs. 6c and d show the relative estimation errors in cdf and pdf across the different quantile values. We see that overall the ray method is better. Both methods are best for computing cdf and pdf values in the middle of the distributions, and they become more erroneous for the same settings as we go out to smaller values in the tails, so to perform better there they will need higher settings (more rays for the ray method, and wider and denser grids for IFFT). The IFFT method is equally accurate on both tails for both elliptical and non-elliptical distributions. The ray method is also equally accurate on both infinite tails of the non-elliptical distributions, but its error rises more sharply on the finite tail of elliptical distributions, for reasons we have discussed before.

Fig. 6e shows the average relative estimation error of the cdf across all quantiles of all the distributions, as a function of the total degrees of freedom of each distribution. We see that the ray method is overall better, but its error climbs with the total d.o.f. This makes sense since this is the number of dimensions of the space in which it is integrating, so a fixed number of rays would be sampling the space more sparsely as the dimension grows, and will miss more features of the integration domain. The error of the IFFT is higher, but more static across d.o.f, since it is always computing a one-dimensional integral of the characteristic function, regardless of the total d.o.f. Fig. 6f shows similar results for computing the pdf, but now the IFFT method is relatively better, and in fact shows some improvement with increasing d.o.f.

Figs. 6g and h show the performance variation as a function of the linear s term. We see that in general, the value of s , whether 0 or across different scales, has little effect on the performance of the methods, although IFFT improves slightly with higher s , as particularly visible for the pdf. This could be because the factor of $e^{-s^2 t^2 / 2}$ in the characteristic function $\phi(t)$ suppresses its tails

and shrinks its width, so it is captured better by an inverse Fourier transform with the same grid span and density.

m is just an offset and we have checked that it has no bearing on performance of either of the methods, so we don't plot it here.

In summary, we see that across a wide sample of distributions, the ray method is overall better than IFFT for computing the cdf and pdf for the same speed, except in the finite tail.

7.3 With equal-covariance multinormals

We have introduced three new methods: ellipse, IFFT and ray. The ellipse method comes with error-bounds, so we know exactly where it can be applied with a known accuracy guarantee. We have shown that the IFFT method agrees with previous exact methods in the body of the distribution, and does not claim high accuracy far in the tails. The ray method agrees with other methods in the body, and extends far into the tails. What remains to be shown is how correct it is in the far tail, because no other exact method can compute a ground-truth value there in reasonable time. So here we show an accuracy test of the ray-trace method in the far tail, using a special case where the ground-truth value is a manageable number, not too tiny or too large for machine representation, that can be exactly calculated: the discriminability index d' .

d' is a measure of statistical separation between two distributions, and for two multinormals with equal covariance Σ , it is given by the easily-calculable Mahalanobis distance between them: $d' = \sqrt{(\mu_a - \mu_b)' \Sigma^{-1} (\mu_a - \mu_b)}$. In a previous paper,⁷ we had introduced the Bayes discriminability index $d'_b = -2Z(p_e)$ that can be calculated from the classification error rate p_e of any two distributions in general, i.e. by computing the probability of each distribution on the wrong side of the classification boundary. For two equal-covariance multinormals, the classification boundary is a plane between them, and we can use the ray-tracing method to integrate the multinormals on either side of the boundary, and compute the error rate and the corresponding d'_b . In this equal-covariance case, d'_b should equal the Mahalanobis distance d' , so we can use this to test the accuracy of the ray method as we separate the two multinormals far apart, which takes us into the tail. Even though the equal-covariance is a simple case, ray-tracing still uses its full algorithm here, so this is a test for the entire general method.

We take two trivariate normals with the following covariance matrix:

$$\Sigma = \begin{bmatrix} 1 & .5 & .7 \\ .5 & 2 & 1 \\ .7 & 1 & 3 \end{bmatrix}$$

The first one stays at the origin while we move the mean of the second in logarithmic steps from the origin along the $[1 \ 1 \ 1]$ vector. At each step we compute the true d' using the Mahalanobis distance, and we use the ray method to compute the classification error rate \hat{p}_e between the multinormals, and the Bayes discriminability index \hat{d}' from it. Fig. 7 shows the relative inaccuracy in this estimate $\frac{|\hat{d}' - d'|}{d'}$ with increasing distance. We first use the ray method with grid integration in double precision (with a relative tolerance of 10^{-20}) to compute \hat{p}_e down to the double-precision limit `realmin`, which corresponds to $\hat{d}' \approx 75$, already a rarely high value. For small d' (<1), the estimate is slower to

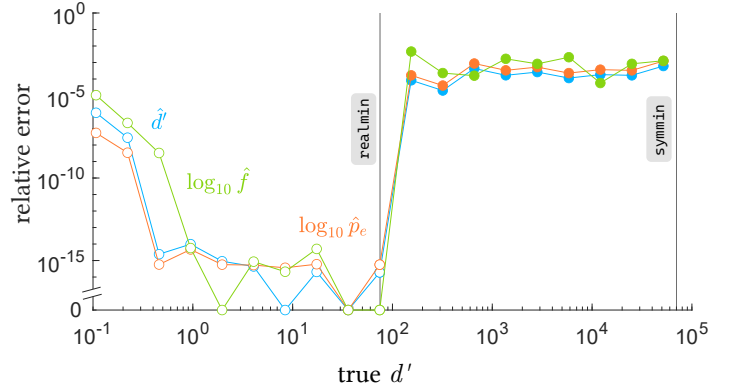


Figure 7: Relative inaccuracies in the ray method's estimates of the discriminability index \hat{d}' and order of magnitude of the classification error rate \hat{p}_e between two multinormals, and the order of magnitude of the probability density \hat{f} at the classification boundary, as we increase the true d' between the multinormals. Open and filled circles are for double precision and variable precision computations respectively. Vertical lines are the limits of computation in double precision (corresponding to an error rate of `realmin`) and variable precision (error rate of `symmin`).

converge to an accurate value, but for large values, which are more relevant when measuring the performance of good classifiers such as ideal observers, the ray method is quite accurate with an error of only around 10^{-15} . In our previous paper,⁷ fig. 8a, we had reported this accuracy up to the double-precision limit of $d' \approx 75$, but now we extend past it with variable precision, using Monte-Carlo integration with 10^3 rays, which yields a stable relative error of only around 0.01% all the way up to a ridiculously large $d' \approx 70,000$ (an error rate of the variable-precision limit `symmin`), beyond which symbolic computation fails.

We can also directly test the accuracy in the ray method's estimate \hat{p}_e of the classification error rate itself, which is essentially a tail cdf, by comparing it to the true known error rate $p_e = \Phi(d'/2)$. We noticed here that in the far tail, where the true p_e was of the order of $10^{-145643038}$ at a point, the estimated \hat{p}_e was around $10^{-145821748}$. So in absolute terms, \hat{p}_e was only $10^{-178710}$ of the true p_e and egregiously wrong, and the estimation error would be 100%. But arguably when comparing such tiny numbers, it is fairer to compare their orders of magnitude instead, which is off by only about 0.1% here. We also notice that similar to our random-sample tests, it is the relative error in the log of the probability or density that is more comparable across scales. So in fig. 7 we show the relative error in the estimate of the order of magnitude of p_e , i.e. $|\log_{10} \hat{p}_e - \log_{10} p_e| / \log_{10} p_e$, and we see that it closely follows the small estimation errors of the d' , which makes sense since d' and p_e are monotonic functions of each other.

We can also test the accuracy of computing the pdf by the ray method here, by computing the probability density of either of the multinormals at the planar classification boundary, which is the same as the density of a standard multinormal at a distance $d'/2$. The ray method is designed to compute the pdf of a *function* of a multinormal though, not the multinormal itself, but we can work around that easily. We take the trivariate standard normal in (x_1, x_2, x_3) , and at each step of d' , we use the ray method to compute the pdf of the 'function' $g(x) = x_1$ at $g = d'/2$ (again

using grid integration with a relative tolerance of 10^{-20} in double precision, and Monte-Carlo integration with 10^3 rays in variable precision). We can compare this density \hat{f} to the known true value of the density at the boundary, $f = \phi(d'/2)$. Like the cdf, this pdf is also tiny in the far tail, so we again look at the estimation error of its order of magnitude: $|(\log_{10} \hat{f} - \log_{10} f) / \log_{10} f|$. We see that the accuracy is comparable to those of \hat{d}' and $\log_{10} \hat{p}_e$.

To compute the tail probability \hat{p}_e and \hat{d}' , with grid integration in double precision it takes from 1 sec (large d') to 1 min (small d') per point, whereas Monte-Carlo integration with 10^3 rays in variable precision takes about 10 min per point. Computing the probability density \hat{f} with grid integration in double precision takes from 2 sec (large d') to 16 sec (small d') per point, whereas Monte-Carlo integration with 10^3 rays in variable precision takes around 2 min per point.

8 Conclusion

In this paper we derived the mapping from generalized chi-square parameters to the parameters of the corresponding quadratic form of a multinormal, and presented two exact (IFFT and ray-trace) methods to compute the cdf and pdf of the distribution, and one approximate method (ellipse) which becomes exact in the limit of the finite tail. These methods are all accompanied by our open-source Matlab software. We compared the performance of these methods against our implementations of previous exact methods by Ruben and Imhof to compute the cdf and pdf for elliptical and non-elliptical distributions. We showed how well they all agree in the middle of the distributions, how far into the tails they can reach, and their accuracy and speed, and presented a table of the best methods to use in different cases. We tested that our two new exact methods match previously published cdf values, and that they are accurate when tested across an array of quantile points on a large set of randomly sampled distributions. We also showed that the high-accuracy ray method can be used to correctly measure large discriminability indices d' between two multinormal distributions.

9 Acknowledgements

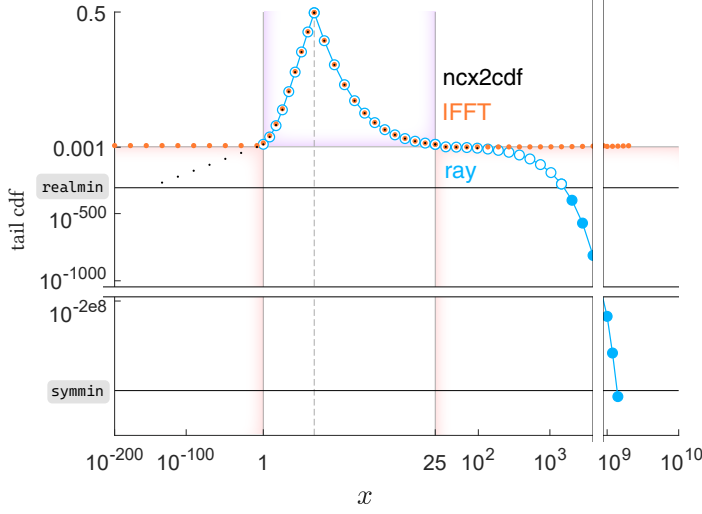
I thank Dr Luis Mendo Tomás (Universidad Politécnica de Madrid) and Dr Andrew D. Horchler (Astrobotic) for their generous help with my Stack Overflow questions on variable precision, and my longtime friend Dr Stefan Eccles (Okinawa Institute of Science and Technology) for backing up my multivariable calculus. I am grateful to my advisor Dr Wilson Geisler (The University of Texas at Austin) for allowing me the time and freedom to work on my own project.

References

- 1 DA Jones. Statistical analysis of empirical models fitted by optimization. *Biometrika*, 70(1):67–88, 1983.
- 2 Hayato Nishi and Ikuho Yamada. Counter-intuitive effect of null hypothesis on moran’s i tests under heterogenous populations (short paper). In *12th International Conference on Geographic Information Science (GIScience 2023)*. Schloss Dagstuhl-Leibniz-Zentrum für Informatik, 2023.
- 3 Housen Li and Frank Werner. Adaptive minimax optimality in statistical inverse problems via solit-sharp optimal lepskii-inspired tuning. *arXiv preprint arXiv:2304.10356*, 2023.
- 4 Nisar Ahmed, Luke Burks, Kailah Cabral, and Alyssa Bekai Rose. Exact consistency tests for gaussian mixture filters using normalized deviation squared statistics. *arXiv preprint arXiv:2312.17420*, 2023.
- 5 Chowdhury Mohammad Rakin Haider, Chris Clifton, and Yan Zhou. Unfair ai: It isn’t just biased data. In *2022 IEEE International Conference on Data Mining (ICDM)*, pages 957–962. IEEE, 2022.
- 6 Chun Yui Wong, Pranay Seshadri, Andrew B Duncan, Ashley Scillitoe, and Geoffrey Parks. Prior-informed uncertainty modelling with bayesian polynomial approximations. *arXiv preprint arXiv:2203.03508*, 2022.
- 7 Abhranil Das and Wilson S Geisler. Methods to integrate multinormals and compute classification measures. *arXiv preprint arXiv:2012.14331*, 2020.
- 8 Jeffrey S Hazboun, Patrick M Meyers, Joseph D Romano, Xavier Siemens, and Anne M Archibald. Analytic distribution of the optimal cross-correlation statistic for stochastic gravitational-wave-background searches using pulsar timing arrays. *arXiv preprint arXiv:2305.01116*, 2023.
- 9 Bruce Allen and Joseph D Romano. Hellings and downs correlation of an arbitrary set of pulsars. *Physical Review D*, 108(4):043026, 2023.
- 10 Stephan Weiss, Connor Delaosa, James Matthews, Ian K Proudler, and Ben A Jackson. Detection of weak transient signals using a broadband subspace approach. In *2021 Sensor Signal Processing for Defence Conference (SSPD)*, pages 1–5. IEEE, 2021.
- 11 Yao-Wen Hsu. Statistical model for approximating gains of arrays with unequal normally distributed errors. *IEEE Transactions on Antennas and Propagation*, 70(12):11653–11664, 2022.
- 12 Andrew Graff and Todd E Humphreys. Purposeful co-design of ofdm signals for ranging and communications. *arXiv preprint arXiv:2309.03076*, 2023.
- 13 Fabian Rothmaier, Yu-Hsuan Chen, Sherman Lo, and Todd Walter. A framework for gnss spoofing detection through combinations of metrics. *IEEE Transactions on Aerospace and Electronic Systems*, 57(6):3633–3647, 2021.
- 14 Birendra Kujur, Samer Khanafseh, and Boris Pervan. Optimal ins monitor for gnss spoofer tracking error detection. *NAVIGATION: Journal of the Institute of Navigation*, 71(1), 2024.
- 15 Paolo Manfredi. Probabilistic uncertainty quantification of microwave circuits using gaussian processes. *IEEE Transactions on Microwave Theory and Techniques*, 2022.

- 16 Hanxiao Liu, Yuqing Ni, Xiaofan Wang, and Lihua Xie. Linear attacks against remote state estimation: Performance analysis under an encryption scheme. *IEEE Transactions on Control of Network Systems*, 2024.
- 17 Kristoffer M Frey. *Belief-Space Planning for Real-World Systems: Efficient SLAM-Based Belief Propagation and Continuous-Time Safety*. PhD thesis, Massachusetts Institute of Technology, 2021.
- 18 Tyler Toner, Dawn M Tilbury, and Kira Barton. Probabilistically safe mobile manipulation in an unmodeled environment with automated feedback tuning. In *2022 American Control Conference (ACC)*, pages 1214–1221. IEEE, 2022.
- 19 Spencer Van Koeveering, Yiwei Lyu, Wenhao Luo, and John Dolan. Provable probabilistic safety and feasibility-assured control for autonomous vehicles using exponential control barrier functions. In *2022 IEEE Intelligent Vehicles Symposium (IV)*, pages 952–957. IEEE, 2022.
- 20 Sooyung Byeon, Joonwon Choi, Yutong Zhang, and Inseok Hwang. Stochastic-skill-level-based shared control for human training in urban air mobility scenario. *ACM Transactions on Human-Robot Interaction*, 2023.
- 21 Harold Ruben. Probability content of regions under spherical normal distributions, iv: The distribution of homogeneous and non-homogeneous quadratic functions of normal variables. *The Annals of Mathematical Statistics*, 33(2):542–570, 1962.
- 22 Jean-Pierre Imhof. Computing the distribution of quadratic forms in normal variables. *Biometrika*, 48(3/4):419–426, 1961.
- 23 J Gil-Pelaez. Note on the inversion theorem. *Biometrika*, 38(3-4):481–482, 1951.
- 24 Robert B Davies. Numerical inversion of a characteristic function. *Biometrika*, 60(2):415–417, 1973.
- 25 Egon S Pearson. Note on an approximation to the distribution of non-central χ^2 . *Biometrika*, 46(3/4):364, 1959.
- 26 Huan Liu, Yongqiang Tang, and Hao Helen Zhang. A new chi-square approximation to the distribution of non-negative definite quadratic forms in non-central normal variables. *Computational Statistics & Data Analysis*, 53(4):853–856, 2009.
- 27 Hong Zhang, Judong Shen, and Zheyang Wu. A fast and accurate approximation to the distributions of quadratic forms of gaussian variables. *Journal of Computational and Graphical Statistics*, 31(1):304–311, 2022.
- 28 Pierre Duchesne and Pierre Lafaye De Micheaux. Computing the distribution of quadratic forms: Further comparisons between the liu–tang–zhang approximation and exact methods. *Computational Statistics & Data Analysis*, 54(4):858–862, 2010.
- 29 Dean A Bodenham and Niall M Adams. A comparison of efficient approximations for a weighted sum of chi-squared random variables. *Statistics and Computing*, 26(4):917–928, 2016.
- 30 BK Shah and CG Khatri. Distribution of a definite quadratic form for non-central normal variates. *The Annals of Mathematical Statistics*, pages 883–887, 1961.

Supplementary information



method	smallest prob.		time/point
	lower	upper	
<code>ncx2cdf</code>	10^{-308}	10^{-18}	0.2 ms
IFFT	10^{-3}	10^{-5}	3 ms
○ ray (dp, 10^3 rays)	10^{-5}	10^{-308}	0.5 ms
● ray (vp, 10^3 rays)	—	$10^{-3 \times 10^8}$	23 s

Figure S1: The cdf of a non-central chi-square $\chi_{k=4, \lambda=5}^2$ computed with Matlab's `ncx2cdf`, our IFFT method (with a grid of $N = 5 \times 10^5$ points that spans 100 times the range over which the cdf is being computed), and our ray-trace method with double precision (open circles) and variable precision (filled), similar to fig. 4. We plot the lower tail probability (cdf) till the median (dashed vertical line), and upper tail probability (complementary cdf) beyond it. The middle of the distribution, probabilities > 0.001 (area highlighted purple) is in linear axes, and the tail regions (areas highlighted red) are in double log axes. The vertical and horizontal white stripes are breaks in the axes, to be able to show the end of the upper tail in the bottom-right, which is much farther below. `realmin` = 10^{-308} is the double-precision limit, and `symmin` $\approx 10^{-3 \times 10^8}$ is the variable-precision limit. Any missing dots are where a method wrongly computes the tail probability as 0. The table below shows the orders of the smallest lower (finite) and upper (infinite) tail probabilities reached by the different methods with their respective settings, and their computation times per point. 'dp' and 'vp' mean double and variable precision. `ncx2cdf` implements a straightforward calculation for the special case of the non-central chi-square, whereas IFFT and ray-trace are using their full general-purpose algorithm even in this special case, so are expected to take longer. In summary, for non-central chi-square cdf's, `ncx2cdf` is the best method for the lower tail and center, but in the upper tail the ray method is best.